

The innermost region of the NGC 1023 Group: Insight into its evolution.

D. Bettoni^{1*}, L. Buson¹, P. Mazzei¹ and G. Galletta²

¹*INAF - Osservatorio Astronomico di Padova*

²*Dipartimento di Fisica e Astronomia Università di Padova*

Accepted Received ; in original form;

ABSTRACT

The NGC 1023 group is one of the most studied nearby groups. We want to give an insight into the evolution of its innermost region by means of ultraviolet observations and proper models. We used the FUV and NUV GALEX archival data as well as a large set of SPH simulations with chemo-photometric implementation. From the UV observations we found that several, already known, dwarf galaxies very close to NGC 1023 are also detected in UV and two more objects (with no optical counterpart) can be added to the group. Using these data we construct exhaustive models to account for their formation. We find that the whole SED of NGC 1023 and its global properties are well matched by a simulation which provides a minor merger with a companion system 5 times less massive. The strong interaction phase started 7.7 Gyr ago and the final merger 1.8 Gyr ago.

Key words: galaxies: structure — galaxies: individual: NGC 1023

1 INTRODUCTION

The NGC 1023 group is one of the most extensively systems studied (300 related references are listed in the NASA/IPAC Extragalactic Database). The first large scale study of it has been performed by Tully (1980). Later on the presence of several outstanding dwarf galaxies drew the attention of Davies & Kinman (1984) who studied in detail four of them in the optical bands.

The most peculiar feature of NGC 1023 is its proximity to the (likely tidally interacting) fainter galaxy NGC 1023A. The latter galaxy appears as a small companion located at the East end of NGC 1023. It appears as a low-luminosity condensation partially embedded in the disc of the larger galaxy. This configuration gives the appearance of an asymmetric spiral arm and led Arp (1966) to include the two galaxies in his Atlas of Peculiar Galaxies as Arp 135. Only later Barbon & Capaccioli (1975) proposed NGC 1023A to be an interacting individual galaxy stressing also its coincidence with a cloud of a neutral hydrogen (HI) identified by Sancisi et al. (1984). Additional, more recent HI observations confirming the Sancisi's results (presence of tails and bridges) has been performed by Morganti et al. (2006). The separation (and different stellar population) of the two objects is assured today also by the UV images of the GALEX satellite (Morrissey et al. 2007). In particular NGC 1023A appears to be an irregular galaxy close to the

SB0 NGC 1023. Moreover the surface brightness, FUV and NUV GALEX profiles of NGC 1023 are included in the Ultraviolet Atlas of Nearby Galaxies of Gil de Paz et al. (2007).

Current programs (e.g. Trentham & Tully 2009) are intended to explore the NGC 1023 environment in order to detect the faintest candidate dwarfs (and establish their possible membership to the group); the outcome of such research could indeed help to clarify, for instance, the so called fundamental missing satellite problem. Moreover NGC 1023 looks to be the first known S0 for which a proper kinematical approach based on PNe (Cortesi et al. 2011) has shown that it likely originates from the secular evolution of a parent spiral galaxy instead of a more disruptive fast merger.

In this paper we analyze UV data in the central region of the group and we use them to characterize its core with SPH simulations. These are used also to investigate the dark matter distribution in the group environment as not confined in the haloes of the single galaxies. The work is structured as follows: section 2 gives a detailed description of the dominant galaxy, NGC 1023, while section 3 provides an exhaustive description of the UV photometric analysis of both NGC 1023 and NGC 1023A. The adopted SPH modeling is described in section 4. The conclusions are finally listed in section 5.

* E-mail: daniela.bettoni@oapd.inaf.it

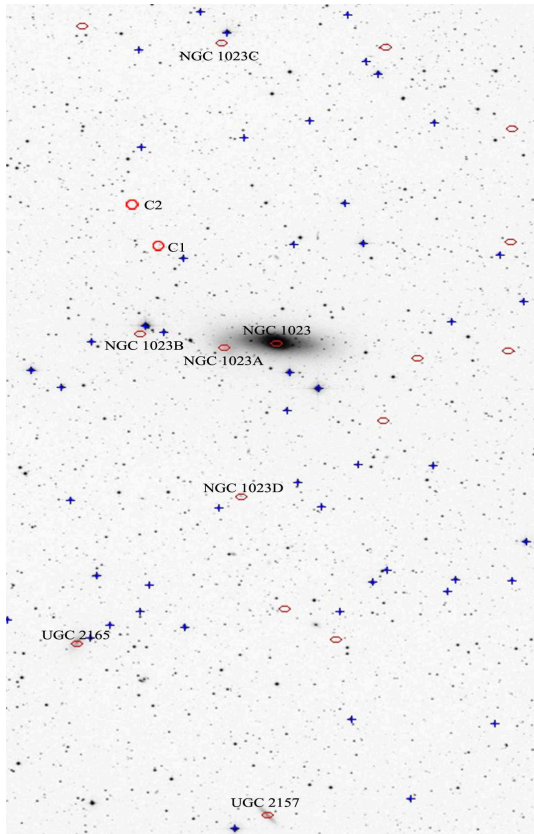


Figure 1. GALEX Identification of the galaxies belonging to the centre of the group. It includes known galaxies from Davies & Kinman (1984) and Trentham & Tully (2009) and newly discovered UV-bright fainter blobs identified as C1 and C2.

2 NATURE OF NGC 1023

NGC 1023 is an almost edge-on lenticular galaxy, classified as SB0 by most catalogues (e.g. RC3; De Vaucouleurs et al. 1991), at an estimated distance of 11.4 Mpc (Tonry et al. 2001). It belongs to a sparse group, rich in spirals, and is the brightest member of the LGG 70 group (Garcia 1993). In the optical images (The Carnegie Atlas 1994) the galaxy appears to be composed of a faint stellar disk, a inner and brighter lens and a bar at $\sim 45^\circ$ from the apparent disk major axis. A central nuclear disk is also present, with relatively young stars (cf. Debattista et al. 2002). From optical line index measurements (Borson et al. 2011, their Table 1) derive a velocity dispersion of 210 km/s and a stellar age of 4.7 Gyr.

The redshift difference with the companion NGC 1023A is $\Delta V = 127 \pm 30$ km s $^{-1}$ (Capaccioli et al. 1986) and the projected distance ~ 7.6 kpc (Barbon & Capaccioli 1975; adopted $H_0 = 75$ km s $^{-1}$ Mpc $^{-1}$). In bluer and deeper images the smaller galaxy exhibits some luminous knots that are consistent with a late-type dwarf galaxy.

3 UV PHOTOMETRY

We used FUV and NUV background-subtracted, de-archived intensity images from the GALEX pipeline. In order to estimate the uncertainties of UV (AB) magnitudes, we propagated Poisson statistical errors on source and back-

ground counts. In addition to the statistical error, we added an uncertainty to account for systematic inaccuracies in the zero-point of the absolute calibration of 0.05 and 0.03 mag for FUV and NUV respectively (Morrissey et al. 2007).

FUV and NUV magnitudes have been computed as

$$m(AB)_{UV} = -2.5 \times \log CR_{UV} + ZP$$

where CR is the dead-time corrected, flat fielded count rate, and the zero points are $ZP = 18.82$ and $ZP = 20.08$ in FUV and NUV respectively (Morrissey et al. 2007). We corrected UV magnitudes by adopting a foreground reddening from Schlegel et al. (1998) for both NGC 1023 and NGC 1023A, namely $E(B-V) = 0.061$. With reference to the extinction curve of Savage & Mathis (1979), this translates into the extinction values $A_{NUV} = 0.56$ and $A_{FUV} = 0.49$ respectively, adopting $\lambda_{eff} = 2267$ Å and 1516 Å for the two above filters.

For our study, first we derive the photometric parameters of NGC 1023 and NGC 1023A and as a second step we cross-correlate the Trentham & Tully (2009) sample of objects with the GALEX photometric catalogue. We found 9 matches (together with NGC 1023 and NGC 1023A) over 28 objects. All the galaxies with know redshift are detected in UV bands while only two (namely NGC1023-15 and NGC1023-17) of the dwarfs listed in Trentham & Tully (2009) have UV emission. In addition to these galaxies we discovered two new objects, identified as C1 and C2. Our GALEX identification of the galaxies, as listed in Davies & Kinman (1984) and Trentham & Tully (2009), are shown in Fig. 1. Both FUV and NUV surface photometry have been performed using IRAF¹ STSDAS ELLIPSE routine. ELLIPSE computes a Fourier expansion for each successive isophote (Jedrzejewski 1987), resulting in the surface photometric profiles.

All corrected magnitudes m_{ABS} ' of NGC 1023, NGC 1023A, and Davies & Kinman's and Trentham & Tully (2009) objects are given in Table 1. In Figures 2,3 we show the NUV, FUV and POSS2 R images of all the objects we have detected (in NUV or FUV). We computed the ultraviolet integrated photometry (FUV+NUV) of each UV-bright source and the color profiles of the two brightest galaxies, namely NGC 1023 and NGC 1023A (Fig 4). Integrated photometric properties are given in Table 1 while photometric parameters for the fits are listed in Table 2. Errors in total magnitudes were obtained from the correlation coefficient of the model fit vs. the observed values.

We fitted the luminosity profiles of NGC 1023 assuming two-components: a bulge following an $r^{1/4}$ law, and an exponential disc. The inner regions of the profiles, affected by the GALEX PSF ($\sim 5''$), were excluded in performing interpolation. The lens and bar are not visible in UV images and the ellipse interpolations find constant ellipticity and P.A. values. In the case of NGC 1023 they are $\epsilon \sim 0.23$ (NUV) and 0.12 (FUV); P.A. $\sim 80^\circ$ (NUV) and 83° (FUV). The values of the bulge effective radii in FUV and NUV reported in Table 1 are quite similar and are in agreement with those found by optical photometry in R band, reported in

¹ IRAF is written and supported by the IRAF programming group at the National Optical Astronomy Observatories (NOAO). NOAO is operated by the Association of Universities for Research in Astronomy (AURA), Inc. under cooperative agreement with the National Science Foundation.

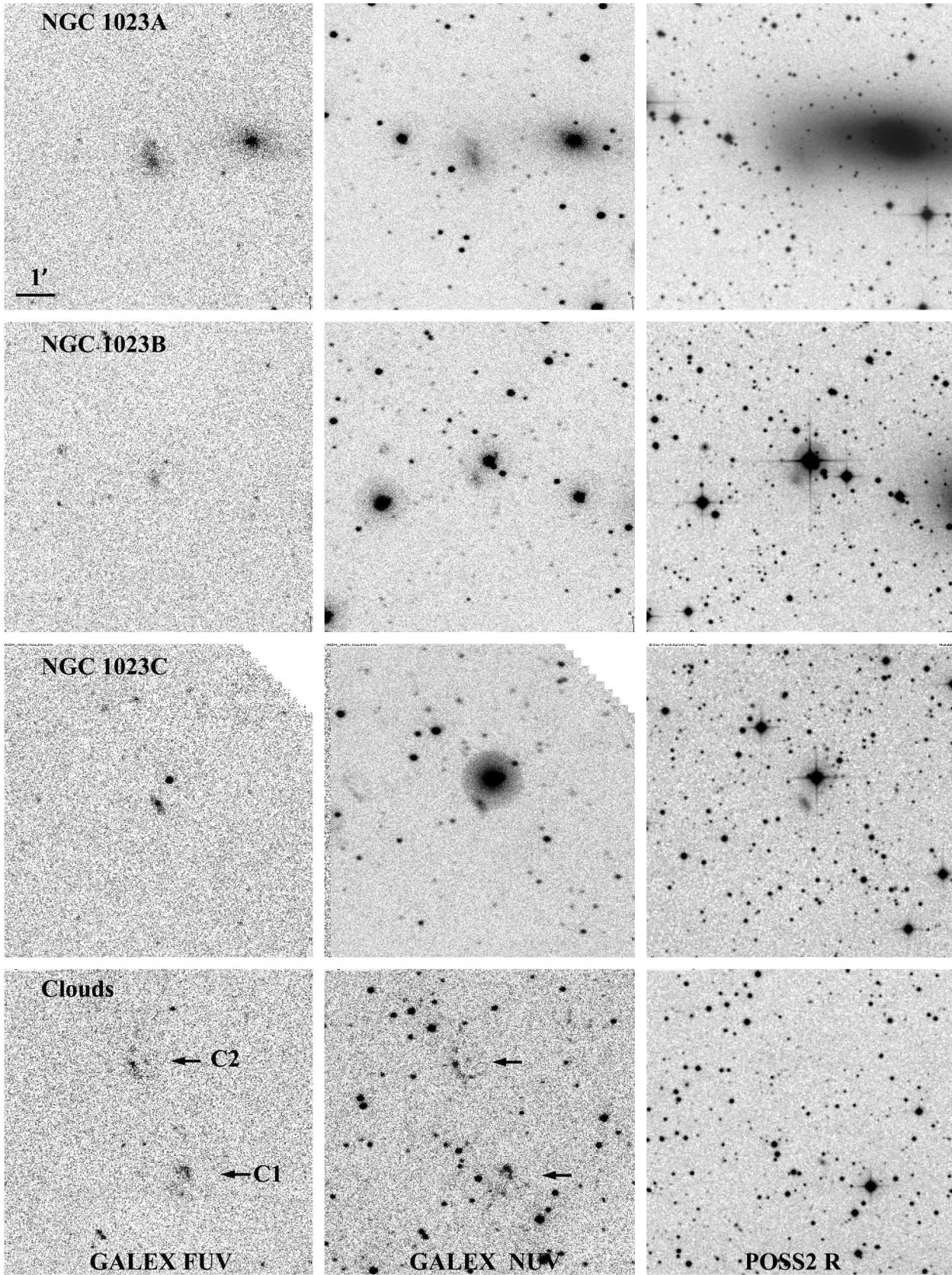


Figure 2. Images of the galaxies belonging to the centre of the group. This includes all galaxies from Davies & Kinman (1984), the galaxies in Trentham & Tully (2009) here detected in FUV or NUV and the newly discovered UV-bright fainter blobs, C1 and C2. All panels have the same size with North at the top and East left.

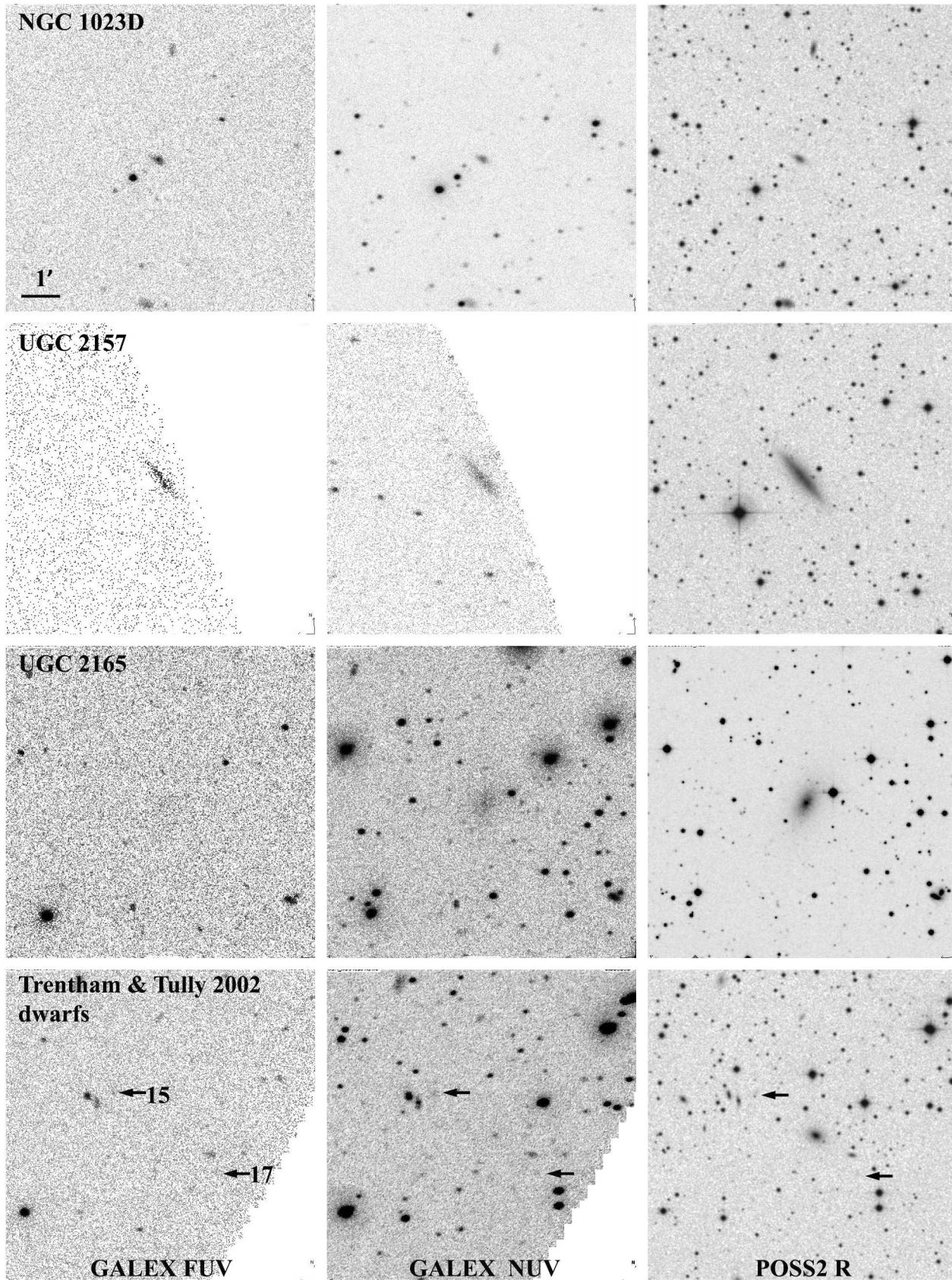


Figure 3. Images of the galaxies belonging to the centre of the group. This includes all galaxies from Davies & Kinman (1984), the galaxies in Trentham & Tully (2009) here detected in FUV or NUV and the newly discovered UV-bright fainter blobs, C1 and C2. All panels have the same size with North at the top and East left.

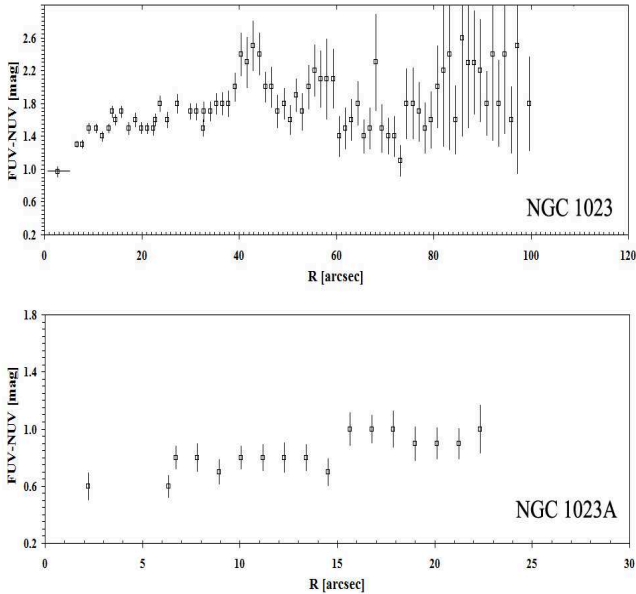


Figure 4. FUV-NUV colors for NGC 1023 and NGC 1023A . Note in the lower panel the bluer (FUV-NUV) color of the whole galaxy body, when compared to the dominant galaxy NGC 1023.

the work of Noordermeer et al. (2005): $r_e(\text{bulge})=32''$. The stellar disk, when observed in red light, appears larger, with an $r_e(\text{disk})=62''$ compared to values lower than $50''$ found in the UV. The FUV-NUV color profile (top panel of Fig. 4) indicate that the nucleus is bluer that the external regions. This is confirmed also by the NUV-r color profile plotted in Fig. 5 together with the FUV-r. The r data were derived from Noordermeer et al. (2005).

Both UV profile components can be fitted in NGC 1023A with an exponential disk. The routine ELLIPSE gives almost constant ellipticity and position angles. They are: $\epsilon \sim 0.45$ (NUV) and 0.38 (FUV), and $P.A \sim 16^\circ$ (both in NUV and FUV). The effective radii and surface brightness are listed in Table 2 together with the total magnitudes of both galaxies. Integrated photometric properties are given in Table 1 while photometric parameters for the fits are listed in Table 2. Contrary to what observed in NGC 1023 the color profile in NGC 1023A is constant around a value ~ 0.8 .

We measured the UV magnitudes of the two UV emission regions, labeled C1 and C2 (see Fig. 1, 2, 3) inside an aperture of $r=15$ arcsec; the values are listed in Table 1. In Fig. 6 we plot the colors of the main objects in the group. We note that NGC 1023 and NGC 1023A have similar colors, whereas the "dwarfs" NGC 1023B, NGC 1023D, UGC 2157 and especially NGC 1023C are quite bluer in the UV (both in FUV-NUV and NUV-B). UGC 2165 on the contrary is very red, in particular the FUV flux measured can be considered as an upper limit and may indicate a very old stellar population.

3.1 Star formation rate

The present-day Star Formation Rate (SFR) of each UV source can be derived—following Kennicutt (1998)—using its UV continuum luminosity and the relation

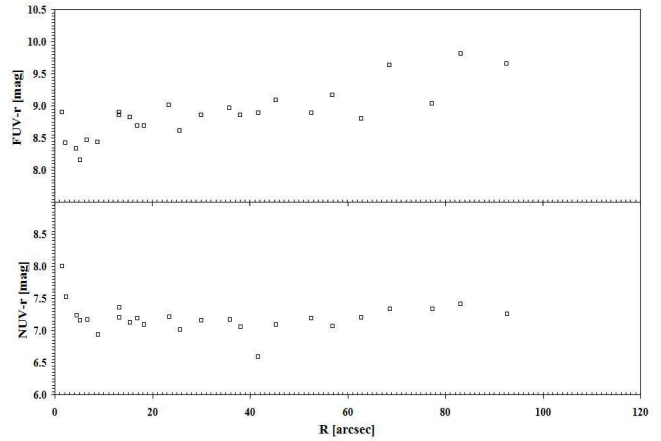


Figure 5. NUV-R and FUV-R color profiles for NGC 1023. Note in the upper panel the much red (FUV-R) color of external regions of the dominant galaxy NGC 1023.

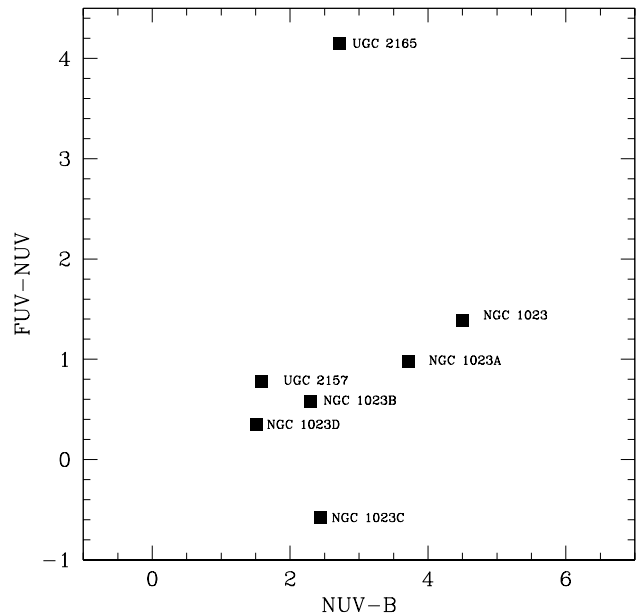


Figure 6. UV-optical two-color diagram of the main dwarf galaxies of the NGC 1023 group.

$$\text{SFR}_{\text{FUV}} (M_{\odot} \text{ yr}^{-1}) = 1.4 \times 10^{-28} L_{\text{FUV}} (\text{ergs s}^{-1} \text{ Hz}^{-1}).$$

Such a relation holds for a Sapeleter's IMF with lower and upper mass limits $0.1 M_{\odot}$ and $100 M_{\odot}$ respectively. We used our total FUV magnitudes to derive the SFRs which are given in Table 1. Using the previous equation we found that the SFR is not null in NGC 1023 although it provides very low values ($2.68 \times 10^{-2} M_{\odot} \text{ yr}^{-1}$). The Spitzer data for the inner regions of this galaxy (Shapiro et al. 2010) indicate no signature of SF. The SFR in the other dwarf galaxies and in the two blobs (C1 and C2) is even lower, with the lowest value, $0.01 \times 10^{-2} M_{\odot} \text{ yr}^{-1}$, for UGC 2165. However their

Table 1. Integrated photometric properties

Object	R.A. (2000)	DEC (2000)	$m_{NUV}(AB)$	$m_{FUV}(AB)$	B mag	R mag	FUV-NUV mag	NUV-B mag	SFR_{FUV} $10^{-2} M_{\odot} \text{ yr}^{-1}$	Radial Vel. km s^{-1}
NGC 1023	40.099	39.065	14.85 ± 0.09	16.24 ± 0.23	10.35	9.14	1.39	4.50	2.68	637
NGC 1023A	40.155	39.056	16.66 ± 0.40	17.64 ± 0.38	12.95	15.30	0.98	3.71	0.73	743
NGC 1023B	40.251	39.073	19.34 ± 0.20	19.92 ± 0.3	17.04	17.34	0.58	2.3	0.09	593
NGC 1023C	40.165	39.380	19.54 ± 0.16	18.96 ± 0.32	17.10	15.13	-0.58	2.44	0.22	903
NGC 1023D	40.137	38.900	18.43 ± 0.22	18.78 ± 0.28	16.92	16.37	0.35	1.51	0.25	695
C1	40.230	39.161	19.49 ± 0.24	19.36 ± 0.32					0.15	
C2	40.258	39.206	19.58 ± 0.3	19.54 ± 0.3					0.13	
UGC 2165	40.314	38.744	18.01 ± 0.16	22.16 ± 0.2	15.29	13.36	4.15	2.72	0.01	740
UGC 2157	40.105	38.563	16.61 ± 0.038	17.39 ± 0.072	15.02	13.67	0.78	1.59	0.92	488
N1023-15	40.087	38.783	19.54 ± 0.31	20.10 ± 0.25		19.71	0.56		0.07	
N1023-17	40.031	38.748	20.26 ± 0.33	20.71 ± 0.12		20.23	0.45		0.04	

Note: B magnitudes of NGC 1023A, NGC 1023B, and NGC 1023D are from Davies & Kinman (1984) and for NGC 1023 from NED, the R magnitudes are from Trentham & Tully (2002)

Table 2. Photometric parameters from the fit of the luminosity profile

Object	Band	m_{tot} mag	r_e (bulge) arcsec	μ_e (bulge) $\text{mag}/''^2$	r_e (disk) arcsec	μ_e (disk) $\text{mag}/''^2$
N1023	NUV	14.85 ± 0.09	34.0 ± 9.5	26.34 ± 0.38	50.00 ± 1.45	27.24 ± 0.07
N1023	FUV	16.24 ± 0.23	32.0 ± 6.6	27.44 ± 0.29	46.00 ± 1.45	28.84 ± 0.09
N1023A	NUV	16.66 ± 0.40	–	–	25.00 ± 2.05	26.34 ± 0.08
N1023A	FUV	17.64 ± 0.38	–	–	20.0 ± 1.55	26.84 ± 0.11

colors (see Fig. 6) are bluer than those of the two brighter galaxies of the group.

4 MODELING

With the aim to match the overall SEDs and the global properties of NGC1023 and NGC1203A in a consistent way with the dynamical properties of the group, we select, from a large set of SPH simulations, one case which gives us insights into the evolution of such a system and the group itself.

Our SPH simulations of galaxy formation and evolution are starting from the same initial conditions as described in Mazzei & Curir (2003) (MC03 in the following) and Mazzei (2003) i.e., collapsing triaxial systems initially composed of dark matter (DM) and gas in different proportions and different total masses.

All the simulations include self-gravity of gas, stars and DM, radiative cooling, hydrodynamical pressure, shock heating, artificial viscosity, star formation (SF) and feedback from evolved stars and type II SNe, and chemical enrichment as in MC03 (and references therein).

They provide the synthetic SED at each evolutionary step. The SED accounted for chemical evolution, stellar emission, internal extinction and re-emission by dust in a self-consistent way, as described in Spavone et al. (2009) and Bettoni et al. (2011); this extends over four order of magnitude in wavelength, i.e., from 0.1 to 1000 μm . So, each simulation self-consistently provides dynamic, morphological, and chemo-photometric evolution. The Initial Mass

Function (IMF) is of Salpeter type with upper mass limit $100 M_{\odot}$ and lower mass limit $0.01 M_{\odot}$ (Salpeter, 1955) (see Curir & Mazzei (1999) and MC03 for a discussion). All the model parameters here adopted had been tuned in previous papers where the integrated properties of simulated galaxies, i.e., colors, absolute magnitudes, mass to luminosity ratios provided by different choices of model parameters after 15 Gyr, had been successfully compared with those of local galaxies (see also Mazzei (2003); Mazzei (2004)). In particular, the IMF choice here provides a slightly higher SFR compared with the other possibilities examined, allows for the lowest feedback strength, and the expected rotational support when disk galaxies are formed. Moreover, as pointed out by Kroupa (2012), its slope is almost the same as the Universal Mass Function which links IMF of galaxies and stars to those of brown dwarfs, planets and small bodies (meteoroids, asteroids) (Binggeli & Hascher 2007).

With respect to MC03, the initial particle resolution here is enhanced to more than 6×10^4 (see below) instead of 2×10^4 , and the time separation between the snapshots halved, 151 Myr.

A new large set of galaxy encounters involving systems with 1:1 mass ratios and different mass ratios have been performed with the same initial conditions as described in MC03 (and references therein). By seeking to exploit a vast range of orbital parameters, we carried out different simulations for each couple of interacting systems varying the orbital initial conditions in order to have, for the ideal Keplerian orbit of two mass points of mass equal to 10^{12} , or $10^{13} M_{\odot}$, the first peri-center separation, p , equal to the ini-

tial length of the major axis of the DM triaxial halo, i.e. 88 kpc for $10^{12} M_{\odot}$, or equal to 1/10, 1/5, and 1/3 of the same axis for $10^{13} M_{\odot}$ encounters. For each of these separations, we changed the eccentricity in order to have hyperbolic orbits of different energy. The spins of the systems are equal (MC03), generally parallel each other, and perpendicular to the orbital plane, so we studied direct encounters. However, some cases with misaligned spins have been also analyzed in order to deepen the effects of the system initial rotation on the results. Moreover, for a given set of encounters with the same orbital parameters we also examined the role of increasing initial gas fractions. All these new simulations will be fully discussed elsewhere (Mazzei, in prep).

A simulation able to match the global properties of NGC 1023 is chosen and discussed below. All the observables, i.e. absolute magnitudes, colors, which correspond to the SED over almost four order of magnitude in wavelength, and mass-to-light luminosity ratios are self-consistently derived from our simulation at the snapshot selected, and successfully compared with the available data.

4.0.1 NGC 1023

The whole SED of NGC 1023 and its global properties are well matched by a simulation which provides a minor merger. The total mass of the primary system is $1 \times 10^{13} M_{\odot}$ with gas fraction 0.01, that-one of the companion is 5 times less with the same gas fraction. So, the starting point is given by two triaxial collapsing systems with total mass $1.2 \times 10^{13} M_{\odot}$, and 60 times less of gas, i.e. $2 \times 10^{11} M_{\odot}$. The mass particle resolution is $5 \times 10^6 M_{\odot}$ for gas and $4.95 \times 10^8 M_{\odot}$ for DM particles. This requires 63838 initial particles. The triaxiality ratio, τ (Warren et al. 1992), is 0.84.

The first pericenter separation, 433 Kpc, corresponds to 1/3 of the major axis of the primary system; the orbit eccentricity is 1.3. and the anomaly corresponds to 200 degrees. The spins of the systems are equal ($\lambda=0.06$, MC03), parallel, so we are dealing with a direct encounter, and both aligned with the shorter of their principal axes.

Stars are born in the inner regions of their halos after 3 Gyr from the beginning. Galaxies grow changing their shapes step by step, as their trajectories are approaching and their halos mixing.

The fit corresponds to a galaxy age of 11.9 Gyr. The strong interaction phase between the systems started 7.7 Gyr ago and the final merger 1.8 Gyr ago. Figure 7 shows the gas accretion history inside a sphere centered on the luminous (V band) centre of the galaxy system with a radius of 50 Kpc. The mass of gas with temperature ≤ 10000 K, which represents the upper limit of the cold gas mass inside the selected radius (its cooling time scale is very shorter than the snapshot time range, 151 Myr), is $9.50 \times 10^8 m_{\odot}$ at the age of our fit (the vertical line in Fig. 7). Such a value well agrees with that derived from eq. (1) of Knapp et al. (1985) using $D=5.93$ Mpc (NED from 3K CMB) and FI, the flux integrated over line, 80 Jy km/s (Noordermeer et al. 2005), i.e., $7.3 \times 10^8 m_{\odot}$; this value is at least a factor 3.7 more using the distance in Morganti et al. (2006, their Table 2, 11.4 Mpc). Figure 8 shows the mass distribution at the selected snapshot inside 50 Kpc, corresponding to $15r_{eff}$ of NGC 1023.

The B band absolute magnitude of the model, $M_B =$

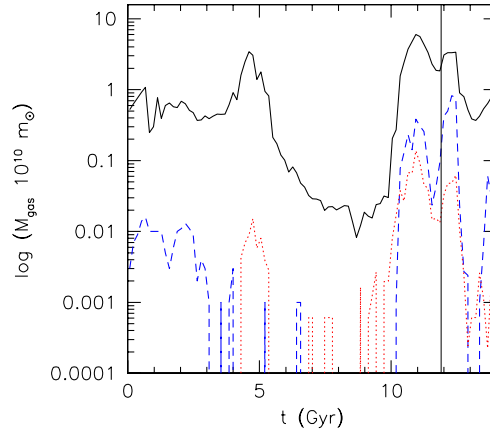


Figure 7. (Black) continuous line shows the evolution of the gas mass inside a radius of 50 Kpc centered on the V band luminous center of the galaxy system; (blue) dashed line corresponds to the gas with temperature ≤ 10000 K, dotted (red) line to the gas with temperature $\geq 10^6$ K. The vertical line emphasizes the age of our fit.

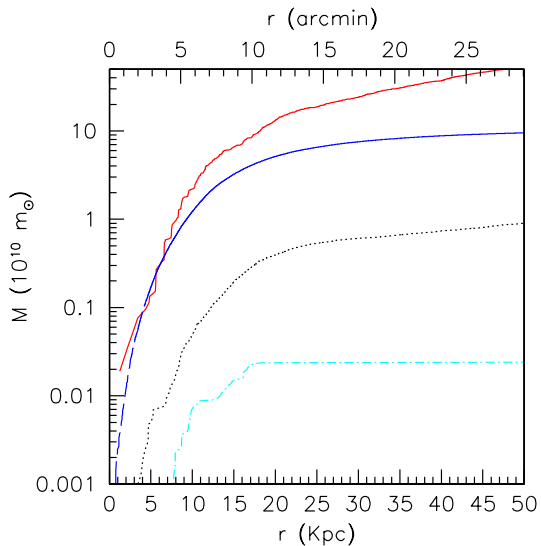


Figure 8. Mass distribution inside a radius of 50 Kpc centered on the V band luminous center of the galaxy system; (red) continuous line corresponds to the DM mass, (blue) long dashed line shows that of stars, (black) dotted line gas, and (cyan) dotted-dashed line cold gas, i.e. gas with $T \leq 10^4$ K.

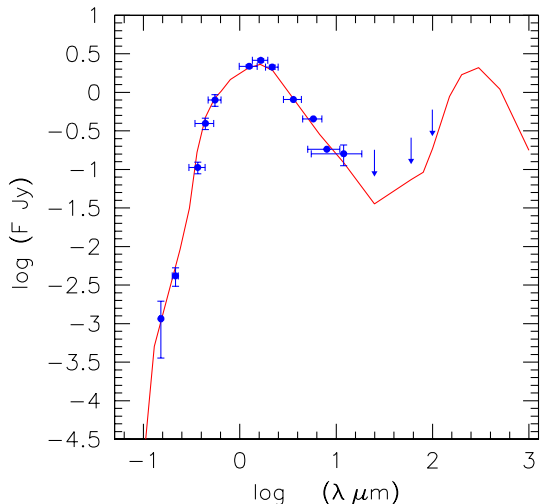


Figure 9. Continuous line (red) show the prediction of our model (see text) for NGC 1023. (Blue) filled circles correspond to data in Table 1 for UV spectral range, from NED in the optical-IR range, and from Pahre et al. (2004) in IR and FIR. Filled triangles show upper limits; error bars account for band width and 3σ uncertainties.

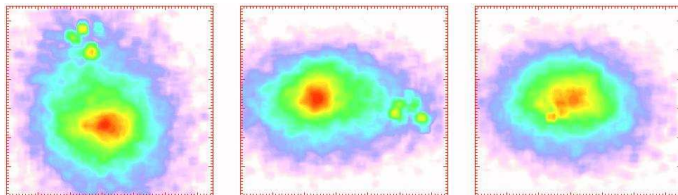


Figure 10. R band contours of XY, YZ and XZ projections of the snapshot that best fits the UV Galax morphology of NGC 1023 (upper panel of Fig 8). Every panel corresponds to 50×50 Kpc and includes sixty equispaced levels for the same density contrast, equal to 100.

-20.35 , agrees with the value in Table 1 of Boroson et al. (2011) and with Table 1 of Emsellem et al. (2007, and references therein, $M_B = -20.42$); R band absolute magnitude, $M_R = -21.95$, agrees with the estimate of Trentham & Tully (2009), $M_R = -22.33$ (their Table 2). Furthermore, all the available data, extending over three order of magnitude in wavelength, are well matched by the SED provided by our simulation, as shown in Fig. 9. The FIR region is not strongly constrained by the data, since upper limits of 25, 60 and $100\mu\text{m}$ fluxes are only available; dust components (warm and cold with PAH as discussed in Mazzei et al. (1992)) with the same average properties as derived by Mazzei et al. (1994) and Mazzei & Curir (2003) for a complete sample of nearby early-type galaxies are included ($r_d=100r_c$, Mazzei et al. (1994)). Figure 10 shows R band maps of different projections of the selected snapshot.

Figure 11 compares, on the same scale, the UV Galax image with superimposed the HI map of NGC 1023, with R map of XY projection as in Fig. 10.

Star populations inside the previous maps are 5.0 Gyr

old in average, in agreement with Boroson et al. (2011) (see Section 2). The luminosity weighted age of the model does not depend strongly on the radius nor on the band, it is 2.5-3 Gyr going from the inner regions up to 50 Kpc.

From the study of Trentham & Tully (2009), the virial mass of the NGC 1023 group inside 315 Kpc (their virial/harmonic radius), is $6.4 \pm 3 \times 10^{12} M_\odot$, and $L_{R_\odot} = 2.0 \times 10^{10} L_\odot$. We predict a total mass of $5.54 \times 10^{12} M_\odot$ with a stellar mass of $1.20 \times 10^{11} M_\odot$, and $L_R = 2.56 \times 10^{10} L_\odot$ inside the same radius.

The instantaneous SFR in the inner region of the simulated galaxy agrees with SAURON results by Shapiro et al. (2010) who measure $\text{SFR} \sim 0 M_\odot \text{ yr}^{-1}$ (see Section 3.1), moreover the total SFR at the selected snapshot, $0.045 M_\odot \text{ yr}^{-1}$, is in well agreement with our estimates from FUV luminosity. Note that to compare these values with those in Table 1 a multiplying factor of ~ 2.4 has to be applied to the data in such a table to account for the lower mass limit of our simulation.

Figure 12 compares our predicted average velocity distribution of stars at each galaxy radius with the same from the data in Fig. 4 of Cortesi et al. (2011). Velocities from our simulations are higher than 7%; such a reduction factor allow us to account for the inclination angle of NGC 1023 that is $\sim 70^\circ$. Note that the green line in Fig. 12 corresponds to the average velocity distribution of planetary nebulae; we select their velocities along the major axis of such a galaxy ($\text{PA}=90^\circ$) accounting for a recession velocity of 637 km/s.

5 CONCLUSIONS

First, we reanalyzed the inner group NGC 1023 by means of deep GALEX images. So we extend to UV range the detailed optical observations of both the four dwarfs studied by Davies & Kinman (1984) and the sample of Trentham & Tully (2009). These observations led to the discovery of two other very faint UV-emitting objects, possibly members of the group itself (see Fig. 3 and Table 1). All the five dwarfs show NUV-B colors bluer than those of the two brighter members of the group. In particular UGC 2165 is very faint in FUV showing extremely red FUV-NUV colors.

Moreover, with the aim at matching the specific overall SEDs and the global properties of NGC1023 and NGC1203A in a consistent way with the dynamical properties of the group, we select, from a large set of SPH simulations, one case which gives us insights into the evolution of such a system and the group itself. Such SPH simulations of galaxy formation and evolution are starting from a collapsing triaxial systems initially composed of dark matter (DM) and gas in different proportions and different total masses. These simulations allowed to investigate the DM distribution in the group environment finding that this is not confined to the halo of single galaxies.

The whole SED of NGC 1023 and its global properties are well matched by the simulation which provides a minor merger, 1:5 ($M_{\text{sat}}/M_{\text{primary}}$). The merger phase started 1.8 Gyr before the selected snapshot. The whole outcome of the model is in strict agreement with Trentham & Tully (2009) results: their estimate of the the R band absolute magnitude is $M_R = -22.33$ to be compared with our $M_R = -21.95$. In addition from their study of the NGC 1023 group, the

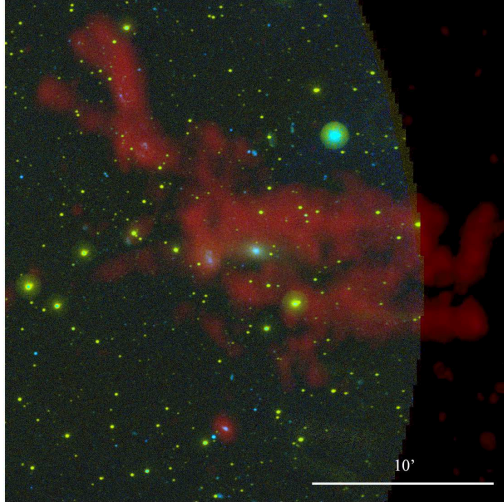


Figure 11. HI band image (red) of NGC 1023 superimposed to the UV GALEX image (*top*), on the same scale (50x50Kpc), with isodensity contours (*bottom*) from our simulation (see text). The simulated image correspond to R band contours of XY projection as in Fig. 7. Note the complex structure of neutral gas in the surroundings of NGC 1023.

virial mass inside 315 Kpc (their virial/harmonic radius), is $6.4 \pm 3 \times 10^{12} M_{\odot}$, and $L_R = 2.0 \times 10^{10} L_{\odot}$, according to our prediction of a total mass of $5.54 \times 10^{12} M_{\odot}$ with a stellar mass of $1.20 \times 10^{11} M_{\odot}$, and $L_R = 2.56 \times 10^{10} L_{\odot}$ inside the same radius.

Looking at its evolution, we predict the group more loose and poor, still no-virialized when the final merger phase is not yet begun, 2 Gyr before our fit, which corresponds to an age of 11.9 Gyr. B and R luminosities are almost the same as at the age of the fit, but there is 20% less mass within the same reference radius, i.e. 315 Kpc (Trentham & Tully 2009). Furthermore, B and R luminosities reduce by 1 and 0.5 mag respectively 2 Gyr after the age of our fit, the total mass being the same.

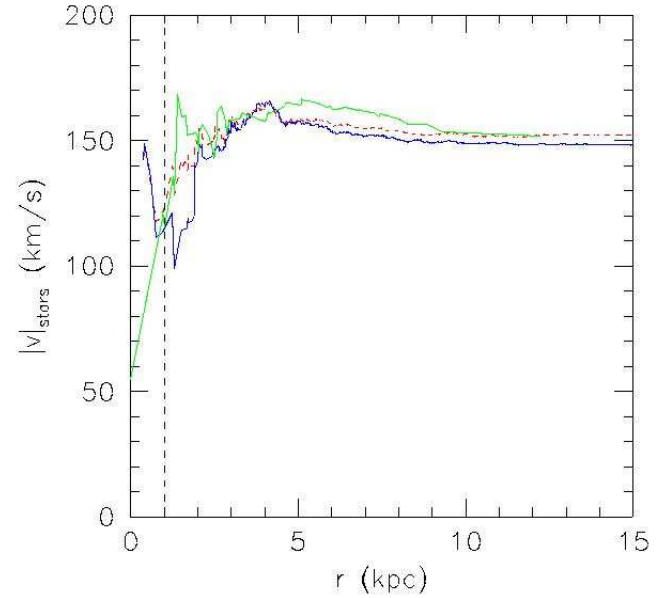


Figure 12. Star absolute velocity distribution at the selected snapshot. Velocities of star particles are computed in their center of mass (red dashed line) and averaged at each galaxy radius; (blue) continuous line shows the same but weighted on V luminosity. The green line corresponds to the average velocity distribution of planetary nebulae. Vertical dashed line corresponds to the inner region ($R \leq 1$ Kpc) where model sampling could affect the results.

ACKNOWLEDGMENTS

We thank the referee Dr. N. Trentham whose comments greatly improved the paper. We acknowledge the financial contribution from University of Padova (ex 60%) and the agreement ASI-INAF I/009/10/0. GALEX is a NASA Small Explorer, launched in April 2003. GALEX is operated for NASA by California Institute of Technology under NASA contract NAS-98034.

REFERENCES

- Arp, H. 1966, ApJS, 14, 1
- Barbon, R., & Capaccioli, M. 1975, A&A, 42, 103
- Bettoni D., Galletta, G., Rampazzo, R., Marino, A., Mazzei, P. & Buson, L. M. 2011, A&A, 534, A24
- Binggeli, B. & Hascher, T. 2007, PASP, 119, 592
- Boroson, B., Dong-Woo, K., & Fabbiano, G. 2011, ApJ 729, 12
- Capaccioli, M., Lorenz, H., & Afanasjev, V. L. 1986, A&A, 169, 54
- Cappellari, M., Emsellem, E., Bacon, R. et al. 2007, MNRAS, 379, 418
- Cortesi, A., Merrifield, M. R., Arnaboldi, M., et al. 2011, MNRAS, 414, 642
- Curir, A., Mazzei, P. 1999, , New Astron., 4, 1
- Davies, R. D., & Kinman, T. D. 1984, MNRAS, 207, 173

- Debattista, V. P., Corsini, E. M., & Aguerri, J. A. L. 2002, MNRAS, 332, 65
- de Vaucouleurs, G., de Vaucouleurs, A., Corwin, H. G., Jr., et al. 1991 (RC3)
- Emsellem, E., Cappellari, M., Krajnovic, D., et al. 2007, MNRAS, 379, 401.
- Garcia, A. M. 1993, A&AS, 100, 47
- Gil de Paz, A., Boissier, S., Madore, B. F., et al. 2007, ApJS, 173, 185
- Jedrzejewski, R. I. 1987, MNRAS, 226, 747
- Jeong, H., Sukyoung, K., Bureau, M. et al. 2009, MNRAS, 398, 2028
- Kennicutt, R. C., Jr. 1998, ARA&A, 36, 189
- Kennicutt, R. C., Jr. 1998, ARA&A, 36, 189
- Knapp, G., Turner, E., Cunniffe, P.E 1985, AJ, 90, 454
- Mazzei, P. 2003, , Mem. Sait, 74, 498
- Mazzei, P., Xu, C., & de Zotti, G. 1992, A&A, 256, 45
- Mazzei, P. & De Zotti, G., Xu, C. 1994, ApJ, 422, 81
- Mazzei, P. & De Zotti, G. 1994, ApJ, 426, 97
- Mazzei, P. & Curir, A. 2003, ApJ, 591, 784: MC03
- Mazzei, P. 2004, Recent Reaserch Dev. in Astron. & Astrop., 1, 457 ed. Pandalari, S.G., Research Signpost; (arXiv:astro-ph/0401509)
- Morganti, R., de Zeeuw, P. T., Oosterloo, T. A., et al. 2006, MNRAS, 371, 157
- Morrissey, P., et al. 2007, ApJS 173, 682
- Noordermeer, E., Merrifield, M. R., Coccato, L., et al. 2005, MNRAS, 384, 943
- Pahre, M.P, Ashby, M. L. N, Fazio, G. G., and Willner, S. P. 2004, ApJSS, 154, 235
- Salpeter, E.E., 1955, ApJ, 121, 161
- Sancisi, R., van Woerden, H., Davies, R. D., & Hart, L. 1984, MNRAS, 210, 497
- Savage, B. D., & Mathis, J. S. 1979, ARA&A, 17, 73
- Schlegel, D. J., Finkbeiner, D. P., & Davis, M. 1998, ApJ, 500, 525
- Shapiro, K. L., Falcón-Barroso, J., van de Ven, G. et al. 2010, MNRAS, 402, 2140
- Spavone, M., Iodice, E., Calvi, R., Bettoni, D., Galletta, G., Longo, G., Mazzei, P. & Minervini, G. 2009, MNRAS, 393, 317
- Tonry, J. L., Dressler, A., Blakeslee, J. P., et al. 2001, ApJ, 546, 681
- Trentham, N., & Tully, R.B., 2009, MNRAS, 398, 722
- Tully, R. B. 1980, ApJ, 237, 390
- Warren, M., Quinn, P., Salmon, J. & Zurek, W. 1992, ApJ, 399, 405